A high-affinity human PD-1/PD-L2 complex informs avenues for small-molecule immune checkpoint drug discovery

Shaogeng Tang[a,b] and Peter S. Kim[a,b,c,1]

[a]Stanford ChEM-H, Stanford University, Stanford, CA 94305; [b]Department of Biochemistry, Stanford University School of Medicine, Stanford, CA 94305; and [c]Chan Zuckerberg Biohub, San Francisco, CA 94158

Contributed by Peter S. Kim, October 14, 2019 (sent for review September 30, 2019; reviewed by Peter G. Schultz and Kevan M. Shokat)

Immune checkpoint blockade of programmed death-1 (PD-1) by monoclonal antibody drugs has delivered breakthroughs in the treatment of cancer. Nonetheless, small-molecule PD-1 inhibitors could lead to increases in treatment efficacy, safety, and global access. While the ligand-binding surface of apo-PD-1 is relatively flat, it harbors a striking pocket in the murine PD-1/PD-L2 structure. An analogous pocket in human PD-1 may serve as a small-molecule drug target, but the structure of the human complex is unknown. Because the CC′ and FG loops in murine PD-1 adopt new conformations upon binding PD-L2, we hypothesized that mutations in these two loops could be coupled to pocket formation and alter PD-1's affinity for PD-L2. Here, we conducted deep mutational scanning in these loops and used yeast surface display to select for enhanced PD-L2 binding. A PD-1 variant with three substitutions binds PD-L2 with an affinity two orders of magnitude higher than that of the wild-type protein, permitting crystallization of the complex. We determined the X-ray crystal structures of the human triple-mutant PD-1/PD-L2 complex and the apo triple-mutant PD-1 variant at 2.0 Å and 1.2 Å resolution, respectively. Binding of PD-L2 is accompanied by formation of a prominent pocket in human PD-1, as well as substantial conformational changes in the CC′ and FG loops. The structure of the apo triple-mutant PD-1 shows that the CC′ loop adopts the ligand-bound conformation, providing support for allostery between the loop and pocket. This human PD-1/PD-L2 structure provide critical insights for the design and discovery of small-molecule PD-1 inhibitors.

PD-1 | PD-L2 | immune checkpoint | drug discovery

Immune checkpoint blockade of programmed death 1 (PD-1) and its ligand 1 (PD-L1) has dramatically increased progression-free survival for many cancers (1–3). The first time that the Food and Drug Administration approved a cancer treatment based on a genetic biomarker rather than the primary site of origin was in 2017, when the anti–PD-1 monoclonal antibody (mAb) drug, pembrolizumab (Keytruda), received approval for use in patients with microsatellite instability-high or mismatch repair-deficient solid tumors (4, 5). Indeed, mAb drugs inhibiting immune checkpoints have ushered in an exciting new chapter in oncology.

Nevertheless, there is a desire for small-molecule inhibitors of immune checkpoints. First, in general, small molecules are expected to penetrate more effectively than mAbs into the tumor microenvironment, perhaps enhancing efficacy (6). In addition, if penetration into the brain is desired, small molecules can be effective (7, 8). Second, there are rare but severe immune-related side effects of checkpoint inhibition that require immediate drug discontinuation (9, 10). Since mAbs have long half-lives in the body (typically weeks) (11), the treatment of such severe immune-related side effects is primarily supportive. Small-molecule checkpoint inhibitors could offer convenient dosing (e.g., once per day) while allowing for prompt drug removal if desired (12). Finally, small-molecule immune checkpoint inhibitors would facilitate cancer treatment in low- and middle-income countries by reducing production costs and eliminating the need for refrigeration during transportation and storage, in contrast to mAbs (13). Despite substantial efforts (14), there are no well-characterized small-molecule ligands for PD-1.

PD-1 has two known endogenous ligands, PD-L1 and PD-L2 (15, 16). These ligands both bind the same surface on PD-1, and current anti–PD-1 mAb drugs block binding of both ligands (17). The available evidence indicates that the primary effect of anti–PD-1 mAb drugs in cancer immunotherapy is mediated through interference with the PD-1/PD-L1 checkpoint pathway.

The ligand-binding surface of human PD-1 is generally flat, lacking pockets considered suitable for binding small molecules (18). However, upon binding to PD-L1, a modest cavity forms on the ligand-binding surface of PD-1 (19). A similar cavity forms in murine PD-1 upon binding of PD-L1 (20). Importantly, when murine PD-1 binds a different ligand, PD-L2 (21), this cavity extends (Fig. 1 *A* and *B*) to a volume comparable to that occupied by established small-molecule inhibitors (22, 23). Unfortunately, this murine structure is insufficient to provide a structural model for

Significance

Immune checkpoint blockade of programmed death-1 (PD-1) by monoclonal antibody drugs has transformed the treatment of cancer. Small-molecule PD-1 drugs have the potential to offer increased efficacy, safety, and global access. Despite substantial efforts, such small-molecule drugs have been out of reach. We identify a prominent pocket on the ligand-binding surface of human PD-1 that appears to be an attractive small-molecule drug target. The pocket forms when PD-1 is bound to one of its ligands, PD-L2. Our high-resolution crystal structure of the human PD-1/PD-L2 complex facilitates virtual drug-screening efforts and opens additional avenues for the design and discovery of small-molecule PD-1 inhibitors. Our work provides a strategy that may enable discovery of small-molecule inhibitors of other "undruggable" protein–protein interactions.

Author contributions: S.T. and P.S.K. designed research; S.T. performed research; S.T. contributed new reagents/analytic tools; S.T. and P.S.K. analyzed data; and S.T. and P.S.K. wrote the paper.

Reviewers: P.G.S., Scripps Research Institute; and K.M.S., University of California, San Francisco.

Competing interest statement: The authors declare a competing interest. S.T. and P.S.K. are named as inventors on a provisional patent application filed by Stanford University and the Chan Zuckerberg Biohub related to the data presented in this work.

Data deposition: Coordinates and structure factors have been deposited in the RCSB Protein Data Bank (http://www.rcsb.org) under PDB ID codes 6UMT for the human PD-1$^{N74G\ T76P\ A132V}$ / PD-L2^{IgV} complex, 6UMU for apo-PD-1$^{N74G\ T76P\ A132V}$, and 6UMV for apo-PD-1$^{T76P\ A132V}$. Structures are available immediately at https://peterkimlab.stanford.edu.

[1]To whom correspondence may be addressed. Email: kimpeter@stanford.edu.

This article contains supporting information online at https://www.pnas.org/lookup/suppl/doi:10.1073/pnas.1916916116/-/DCSupplemental.

First published November 14, 2019.

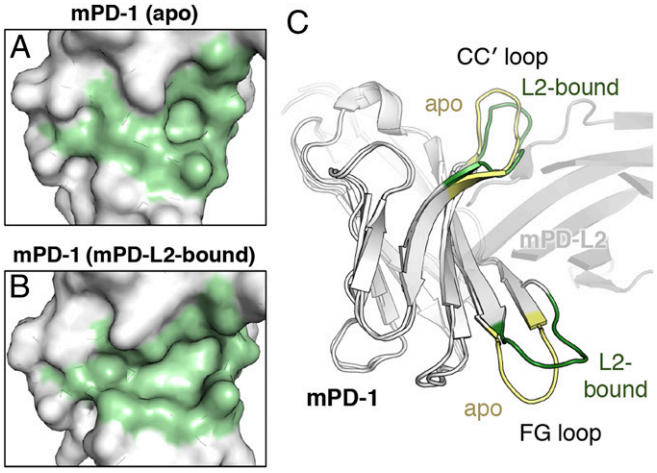

Fig. 1. Conformational changes in murine PD-1 upon binding PD-L2. (*A* and *B*) Close-up views of space-filling models of murine apo-PD-1 (PDB ID code: 1NPU) (*A*) and murine PD-L2–bound murine PD-1 (PDB ID code: 3BP5) (*B*). The hydrophobic ligand-binding interface on PD-1 (pale green) forms a large pocket when murine PD-1 binds to PD-L2. (*C*) Overlay of ribbon diagrams of the murine apo-PD-1 (PDB ID code: INPU) and the PD-L2–bound murine PD-1 (PDB ID code: 3BP5). The CC′ loops and the FG loops adopt different conformations and are highlighted for the apo (pale yellow) and PD-L2 bound (dark green) structures. mPD-1, murine PD-1; mPD-L2, murine PD-L2.

the analogous pocket in the human PD-1/PD-L2 complex, as the human and murine PD-1 proteins share sequence identities of only 63% (24).

Although the murine PD-1/PD-L2 structure was determined over a decade ago (21), the structure of the human complex has not been reported. Our previous attempts to obtain diffraction-quality crystals of the human PD-1/PD-L2 complex were unsuccessful. Analyses of earlier structural studies (21, 24) revealed that formation of cavities on the ligand-binding surface of PD-1 is accompanied by changes in the structures of the CC′ and FG loops (Fig. 1*C*). We therefore hypothesized that substitutions in these loops could have an allosteric effect on the conformations of PD-1 in the pocket region and alter its affinity for PD-L2. Using deep mutational scanning (25, 26) and yeast surface display (27), we selected for CC′ and FG loop variants of human PD-1 with enhanced PD-L2 binding. We identified a triple-mutant PD-1 that binds PD-L2 with nanomolar affinity and is amenable to crystallization, both alone and as a complex. The resulting X-ray crystal structures confirm that a prominent pocket forms in human PD-1 upon binding of PD-L2 and support the notion of allostery between the pocket and the CC′ and FG loops. The pocket identified here in human PD-1 can serve as a template for virtual drug discovery (28) and opens up additional avenues for the discovery of small-molecule PD-1 inhibitors.

Results

Engineering Human PD-1 Loop Variants with Enhanced PD-L2 Affinity. Substantial efforts by us and others (29) to crystallize the human PD-1/PD-L2 complex were previously unsuccessful. Earlier studies (18, 19, 21) indicated that the PD-1 ligand-binding interface consists of a hydrophobic core, the CC′ loop, and the FG loop (Fig. 2*A*), and that formation of a complex with ligands results in loop movement and pocket formation in the hydrophobic core. We hypothesized that mutations in these two loops of PD-1 were coupled to pocket formation and could alter PD-1's affinity for PD-L2. Consistent with this hypothesis, we found that polyglycine mutants of these loops in human PD-1 substantially decreased affinities for PD-L2 (*SI Appendix*, Fig. S1 *A* and *B*).

Since we were particularly interested in the structure of the PD-1 pocket when bound to PD-L2, we maintained residues in the hydrophobic core and performed directed evolution exclusively in the CC′ loop (residues 70–78) and the FG loop (residues 127–133) of human PD-1. We used deep mutational scanning (25, 26) to construct loop-variant libraries with trinucleotides encoding each of 20 residues at each position. We next used yeast surface display (27) (*SI Appendix*, Table S1) with a recombinant human PD-L2-human Fc fusion protein as the selection agent (Fig. 2*B*). After two rounds of selection using magnetic-activated cell sorting and fluorescence-activated cell sorting (Fig. 2*C*), we isolated human PD-1 loop-variant clones with single-residue substitutions. Substitutions at two residues were identified in the CC′ loop (N74G and T76P) and at one residue in the FG loop (A132V, A132L) (Fig. 2*D*). In contrast, when we used the same yeast library and selected with PD-L1-Fc, we only isolated the A132 substitutions as high-affinity variants (*SI Appendix*, Fig. S1 *C–E*), suggesting that the N74G and T76P variants are PD-L2–binding specific. We chose PD-1^{T76P} as a template to generate a second PD-1 loop variant library and selected for further enhancement of PD-L2 binding (Fig. 2*C*). As a result, we obtained a PD-1 triple mutant (*SI Appendix*, Fig. S1 *F* and *G*) that contains all three substitutions identified from the first library: N74G, T76P, and A132V.

PD-1 Loop Variants Showed Increased Binding Affinity and Association Kinetics for PD-L2 and PD-L1. To validate the detected enhancement in affinity, we recombinantly expressed and purified human PD-1 and the loop variants, as well as the human PD-L2 and PD-L1 ectodomain proteins. Using bio-layer interferometry, we compared the binding of PD-L2 to wild-type (WT) PD-1 and to the variants (Fig. 2*E* and *SI Appendix*, Fig. S2*A*). WT PD-1 binds PD-L2 with a K_D of 500 nM; the variants all exhibit increased PD-L2 affinity, with K_D values of 170 nM for N74G, 12 nM for T76P, and 69 nM for A132V (Fig. 2*G*). Remarkably, the PD-1 triple mutant has a K_D of 2.6 nM for PD-L2, constituting a ∼200-fold increase in affinity (Fig. 2*G*). The triple mutant also shows substantially higher affinity for PD-L1 (Fig. 2 *F* and *G*). The A132V mutant has higher affinity for PD-L1, consistent with previous reports (21, 29–31), but the N74G and T76P single mutants have minor effects (Fig. 2 *F* and *G* and *SI Appendix*, Fig. S2 *B* and *C*). Thus, this human PD-1 triple mutant exhibits a potent enhancement of binding affinity for both PD-L1 and PD-L2.

Bio-layer interferometry of ligand binding also enabled us to determine association constants (k_{on}). Compared to WT PD-1, all loop variants showed increased k_{on} for binding PD-L2 (Fig. 2*G*). The PD-1 triple mutant underwent a 3-fold increase of k_{on} for PD-L2, and a 14-fold increase for PD-L1 (Fig. 2*G*). These results suggest that these amino acid substitutions in the loops stabilize the ligand-bound state among the conformational ensembles of apo-PD-1 (ref. 32; see, however, ref. 33).

X-Ray Crystal Structure of the Human PD-1/PD-L2 Complex. We then attempted to crystalize the human PD-1/PD-L2 complex using the PD-1 triple mutant. Site-directed mutagenesis was used to remove all N-linked glycosylation sites in each protein in an effort to aid crystallization (*SI Appendix*, Table S2). Coexpression of the PD-1 triple mutant and the immunoglobulin variable (IgV) domain of PD-L2 yielded a stable and 1:1 stoichiometric complex (*SI Appendix*, Fig. S3 *A* and *B*). We successfully obtained crystals of the human PD-1$^{N74G\ T76P\ A132V}$/PD-L2^{IgV} complex and determined an X-ray cocrystal structure at 2.0 Å resolution (Fig. 3*A* and *SI Appendix*, Fig. S3 *C* and *D*). The crystal contains one PD-1/PD-L2 complex per asymmetric unit, with space group $P\ 2_1\ 2_1\ 2_1$ (Table 1) (34). This structure reveals that the human PD-1/PD-L2 complex adopts an overall architecture similar to that previously

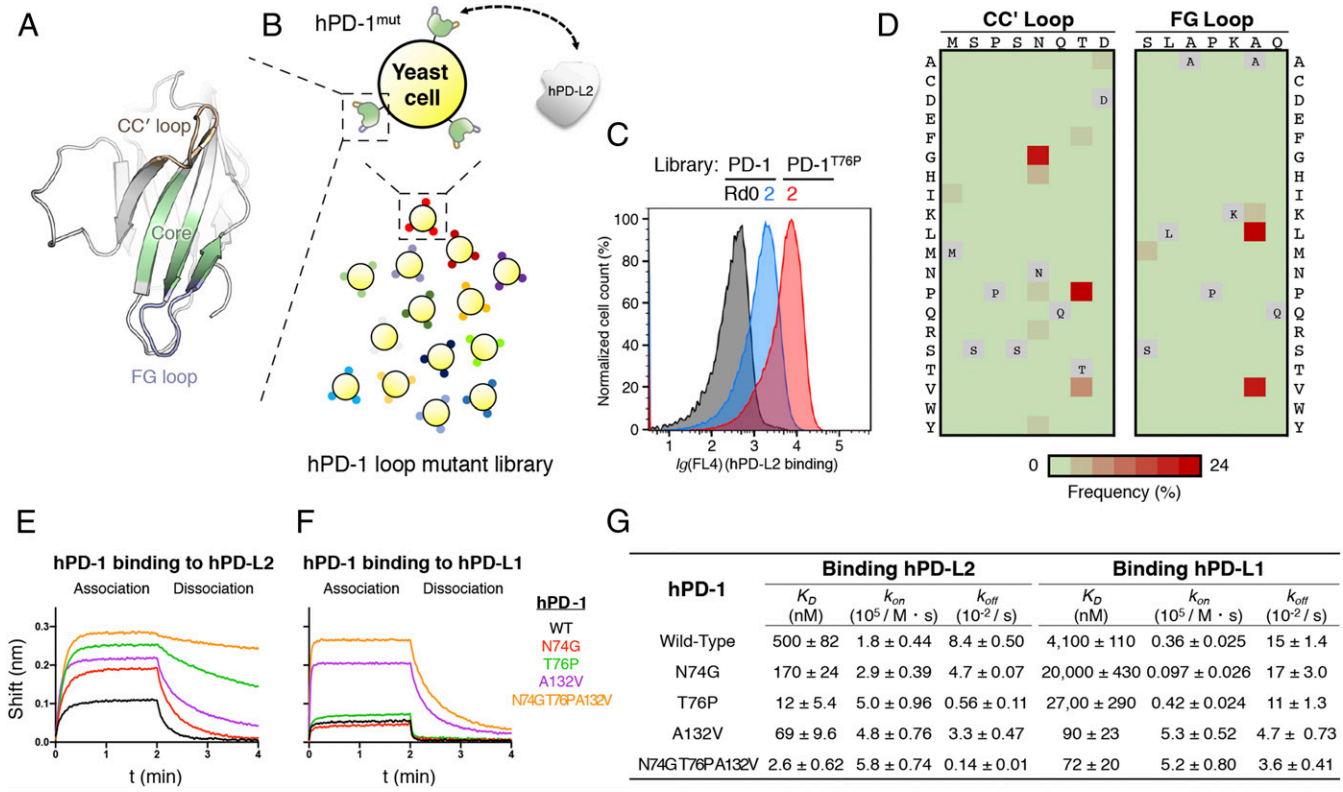

hPD-1	Binding hPD-L2			Binding hPD-L1		
	K_D (nM)	k_{on} (10^5 / M · s)	k_{off} (10^{-2} / s)	K_D (nM)	k_{on} (10^5 / M · s)	k_{off} (10^{-2} / s)
Wild-Type	500 ± 82	1.8 ± 0.44	8.4 ± 0.50	4,100 ± 110	0.36 ± 0.025	15 ± 1.4
N74G	170 ± 24	2.9 ± 0.39	4.7 ± 0.07	20,000 ± 430	0.097 ± 0.026	17 ± 3.0
T76P	12 ± 5.4	5.0 ± 0.96	0.56 ± 0.11	27,00 ± 290	0.42 ± 0.024	11 ± 1.3
A132V	69 ± 9.6	4.8 ± 0.76	3.3 ± 0.47	90 ± 23	5.3 ± 0.52	4.7 ± 0.73
N74GT76PA132V	2.6 ± 0.62	5.8 ± 0.74	0.14 ± 0.01	72 ± 20	5.2 ± 0.80	3.6 ± 0.41

Fig. 2. Engineering PD-1 loop variants with enhanced PD-L2 affinity and association kinetics. (*A*) Ribbon diagram of the human PD-1 ectodomain, highlighting the CC′ loop (wheat), the FG loop (light blue), and the hydrophobic ligand-binding interface (pale green). (*B*) Schematic of yeast surface display of a human PD-1 (hPD-1) loop variant library (colored spheres) and selection for binding of a recombinant human PD-L2 (hPD-L2) ectodomain. (*C*) Overlay of flow-cytometric histograms of the PD-1 loop-variant yeast library at selection rounds 0 (black) and 2 (blue), and the PD-1^{T76P} loop variant yeast library at selection round 2 (red). Yeast cells were stained with 10 nM PD-L2-Fc, followed by Alexa Fluor 647-labeled secondary antibody against human Fc. Yeast cells exhibit enhanced PD-L2-Fc binding after rounds of selection. (*D*) Frequency heatmaps of human PD-1 amino acid substitutions in the CC′ loop (*Left*) and the FG loop (*Right*) after selection round 2 of the PD-1 loop-variant yeast library using PD-L2-Fc. Substitutions of N74G and T76P were identified in the CC′ loop and A132V and A132L in the FG loop. (*E* and *F*) Binding of sensor-loaded PD-1 and the loop variants to 190 nM PD-L2 (*E*) and 1.1 μM PD-L1 (*F*) using bio-layer interferometry. Corresponding PD-1-Fc proteins were loaded on anti-human IgG Fc capture (AHC) biosensors. Association and dissociation were each monitored for 2 min. (*G*) Summary of binding affinity (K_D) and kinetic parameters (association constant k_{on}, dissociation constant k_{off}) for the PD-1 loop variants binding to PD-L2 or PD-L1. Fitting of binding curves was performed in GraphPad Prism 8 using built-in equations of "Receptor binding–kinetics" model. Means and SDs were calculated from three to four independent experiments.

determined for the murine PD-1/PD-L2 complex (21) with a C_α root-mean-square deviation (rmsd) of 3.8 Å. To our knowledge, no human PD-L2 structures have been previously described.

The human PD-1/PD-L2 interface is formed by the front β-sheets of both IgV domains (Fig. 3*B*), burying 1,840 $Å^2$ (14% of the total) of the solvent-accessible surface area. In the interface, notable interacting residues include the three highly conserved aromatics $W110_{L2}$, $Y112_{L2}$, and $Y114_{L2}$ from βG of the PD-L2 IgV domain. The side chains of these residues point into the center of the PD-1 ligand-binding surface (*SI Appendix*, Fig. S4 *A* and *B*). To validate whether the PD-1/PD-L2 interface of the PD-1 triple mutant complex resembles the WT PD-1/PD-L2 interactions, we performed site-directed mutagenesis on several PD-1 and PD-L2 interfacial residues using the natively glycosylated WT proteins. Bio-layer interferometry revealed reduced binding of PD-1 interface mutants to PD-L2, and PD-L2 interface mutants to PD-1 (*SI Appendix*, Fig. S4 *C* and *D*), consistent with our cocrystal structure. The high-affinity loop substitutions of PD-1 localize to the interface (Fig. 3*B*). Among them, T76P and A132V make additional contacts to PD-L2 that likely contribute to the increase in affinity (*SI Appendix*, Fig. S4 *E*–*H*).

X-Ray Crystal Structures of Human Apo-PD-1 Loop Variants. To assist analyses of the conformational changes in PD-1 associated with PD-L2 binding, we crystallized two human apo-PD-1 loop variants (*SI Appendix*, Table S2) and determined X-ray crystal structures at 1.2 Å and 1.4 Å resolution for PD-$1^{N74G\ T76P\ A132V}$ (*SI Appendix*, Fig. S5 *A* and *C*) and PD-$1^{T76P\ A132V}$ (*SI Appendix*, Fig. S5 *B* and *D*), respectively. Crystals of both variants contain a single PD-1 molecule per asymmetric unit, with space group $P\ 3_2\ 2\ 1$ (Table 1). Both PD-1 variants were well defined by the electron density maps, with the notable exception of the CC′ loop discussed further below (*SI Appendix*, Fig. S5 *E* and *F*). Superimposing the apo and PD-L2–bound PD-$1^{N74G\ T76P\ A132V}$ structures resulted in a C_α rmsd of 1.6 Å.

The C′D loop of PD-1 (residues 83–92) is a major part of the pembrolizumab epitope (35–37). This loop is not resolved in earlier structures of human PD-1 in the absence of pembrolizumab (19, 29, 38) but is clear in both of our apo-PD-1 structures. Our results indicate that the conformation of the loop changes substantially upon antibody binding (*SI Appendix*, Fig. S5*G*).

Formation of a Prominent Pocket in Human PD-1 upon Binding PD-L2 with an Architecture Distinct from the Murine Pocket. Our crystal structures of the human PD-1/PD-L2 complex and apo-PD-1 variants allowed us to examine formation of the human PD-1 pocket in the PD-1/PD-L2 interface. Although the human apo-PD-1 variant has a flat ligand-binding interface (Fig. 3*C*),

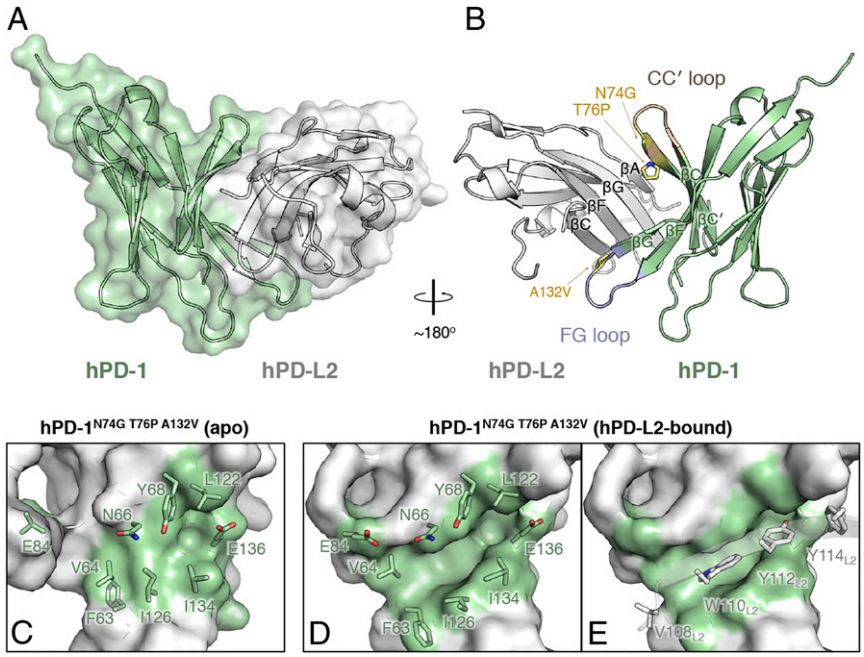

Fig. 3. X-ray crystal structure of the human PD-1/PD-L2 complex reveals a prominent pocket in PD-1. (*A*) Overlay of a space-filling diagram and a ribbon diagram of the complex of human PD-1$^{N74G\ T76P\ A132V}$ (pale green) and PD-L2^{IgV} (gray), showing the overall architecture of the human PD-1/PD-L2 complex. (*B*) Ribbon diagram of a ∼180° rotation view of *A* with the CC′ loop colored in wheat and the FG loop in light blue. The location of the substitutions of N74G, T76P, and A132V are labeled, and their side chains are indicated with sticks (pale yellow). The β-sheets on the interacting faces of each protein are labeled. (*C*–*E*) Close-up views of space-filling models of apo-human PD-1$^{N74G\ T76P\ A132V}$ (*C*) and human PD-L2-bound human PD-1$^{N74G\ T76P\ A132V}$ overlaid with pocket residues shown as sticks (*D* and *E*). In *E*, a ribbon diagram of the βG of PD-L2 is shown with PD-L2–interacting residues overlaid as sticks and labeled with an L2 subscript. A 170 Å^3 funnel-shaped pocket forms (*Left*, entrance; *Right*, exit) when human PD-1 binds PD-L2.

there are rearrangements in this interface upon binding PD-L2. These rearrangements involve residues in βC (F63, V64, N66, Y68), βF (L122, G124, I126), βG (I134, E136), and the C′D loop (E84) to form a deep and extended pocket (Fig. 3*D*). Each of these residues in PD-1 is within 4.4 Å of a PD-L2 residue (*SI Appendix*, Fig. S4*I*). This pocket accommodates PD-L2 side chains including the aromatic residues $W110_{L2}$ and $Y112_{L2}$ (Fig. 3*E*).

Comparison of the PD-1 pockets in the human and murine PD-1/PD-L2 complexes revealed striking differences in pocket geometries. The human pocket adopts an open, funnel-shaped architecture. Compared to the murine pocket (Fig. 1*B* and *SI Appendix*, Fig. S6 *B* and *C*), the human pocket has a wider entrance and a narrower exit (Fig. 3*D*). The distinct pocket geometries arise from at least two factors. First, human PD-1 employs a different subset of interfacial residues to form the pocket than the murine version. Human PD-1 lacks an ordered βC′′ strand and, thus, the open pocket is formed by rearranging residues F63, V64, and E84. In contrast, the murine pocket is closed, with side chains of A81 and S83 forming a boundary (*SI Appendix*, Fig. S6 *A* and *B*). Second, several sequence variations exist among the residues that form the pocket. For example, V64 and Y68 in human PD-1 are substituted with M64 and N68 in murine PD-1, respectively (Fig. 3*D* and *SI Appendix*, Fig. S6*B*). To quantitatively evaluate the pocket dimensions, we measured pocket volumes using POCASA 1.1 (39). The human and murine pockets have volumes of 170 Å^3 and 220 Å^3, respectively. Notably, these pockets are comparable in size to other protein cavities with established small-molecule inhibitors (160–800 Å^3) (22, 23, 40, 41).

We compared our human PD-1/PD-L2 structure (*SI Appendix*, Fig. S6*E*) with the previously determined human PD-1/PD-L1 structure (19) (*SI Appendix*, Fig. S6*F*). Superimposing the two structures resulted in a C_α rmsd of 1.5 Å for PD-1 residues. Binding PD-L1 triggers formation of a much smaller cavity in human PD-1, with a volume of 80 Å^3 (*SI Appendix*, Fig. S6*D*). PD-L1 lacks a large aromatic side chain corresponding to $W110_{L2}$, so the PD-1 rearrangement only involves accommodation of a small subset of the interfacial residues, including the side chain of $Y123_{L1}$, which corresponds to PD-L2 residue $Y112_{L2}$ (*SI Appendix*, Fig. S6 *E*–*H*). These results indicate that the core of the human PD-1 interface has remarkable structural plasticity, with the ability to form pockets with varied dimensions to interact with different PD-1 ligands.

The CC′ Loop in Triple-Mutant PD-1 Adopts a Ligand-Bound Conformation in the Absence of Ligand. We also detected conformational changes in the CC′ and FG loops when human PD-1 binds PD-L2 (Fig. 4 *A* and *B*). Earlier studies reported that the CC′ loop undergoes a substantial conformational change when human PD-1 binds PD-L1 (19, 38). This CC′ loop conformational change is even larger in the human PD-1/PD-L2 structure reported here (Fig. 4*A* and *SI Appendix*, Fig. S7*A*). Strikingly, in the absence of ligands, the CC′ loop conformations of the PD-1 triple and double mutants resemble those of the ligand-bound conformations (*SI Appendix*, Fig. S7*A*). For example, a 4.8 Å shift occurs between the C_α of T76 and P76 in the PD-1 triple mutant of apo-PD-1 (Fig. 4*A*). When the PD-1 triple mutant binds PD-L2, the side chain of P76 maintains the same conformation as the unbound protein (Fig. 4*A*). An increased population of the ligand-bound conformations of the mutant apo-PD-1 proteins is consistent with increased association constants (k_{on}) of the PD-1 variants (Fig. 2*G* and *SI Appendix*, Fig. S2*C*).

In contrast, the conformations of the FG loop are the same in all three apo-PD-1 structures: one with an A132L substitution in

Table 1. Crystallographic data collection and refinement statistics

	PD-1$^{N74G\ T76P\ A132V}$/PD-L2^{IgV}	Apo-PD-1$^{N74G\ T76P\ A132V}$	Apo-PD-1$^{T76P\ A132V}$
PDB ID code	6UMT	6UMU	6UMV
Wavelength, Å	0.979	0.979	0.979
Resolution range, Å	37.5–1.99 (2.06–1.99)	36.5–1.18 (1.23–1.18)	36.5–1.42 (1.48–1.42)
Space group	$P\ 2_1\ 2_1\ 2_1$	$P\ 3_2\ 2\ 1$	$P\ 3_2\ 2\ 1$
Unit cell	41.3 67.8 89.7	46.2 46.2 89.3	46.2 46.2 89.4
	90 90 90	90 90 120	90 90 120
Total reflections	185,797 (11,081)	400,313 (24,984)	171,335 (11,683)
Unique reflections	17,750 (1,645)	36,661 (3,544)	21,301 (2,090)
Multiplicity	10.4 (6.7)	10.9 (7.0)	8.0 (5.6)
Completeness, %	98.6 (90.6)	99.7 (98.8)	99.7 (98.2)
Mean I/sigma(I)	16.1 (2.28)	28.5 (2.79)	23.3 (2.40)
Wilson B-factor	35.8	16.7	21.9
R_{merge}	0.139 (0.723)	0.0521 (0.539)	0.0903 (1.03)
$CC_{1/2}$	0.992 (0.780)	0.999 (0.856)	0.998 (0.769)
CC^*	0.998 (0.936)	1.00 (0.960)	0.999 (0.932)
R_{work}	0.198 (0.290)	0.154 (0.192)	0.161 (0.194)
R_{free}	0.226 (0.337)	0.164 (0.233)	0.189 (0.260)
No. of nonhydrogen atoms	1,769	1,156	1,135
Macromolecules	1,643	1,001	1,048
Water	125	144	82
Protein residues	208	112	116
RMS (bonds), Å	0.014	0.009	0.016
RMS (angles), °	1.91	1.35	1.64
Ramachandran favored, %	100	100	99
Ramachandran outliers, %	0	0	0
Clashscore	4.95	0.99	2.86
Average B-factor	50.5	23.4	30.1
Macromolecules	50.3	21.1	29.4
Solvent	53.7	38.2	39.1

Statistics for the highest-resolution shell are shown in parentheses.

the FG loop (29) and the triple and double mutants described here (*SI Appendix*, Fig. S7*B*). Upon binding PD-L1 (19), there are no substantial conformational changes in the FG loop (Fig. 4*B*). There is, however, a drastic shift in the FG loop conformation upon binding PD-L2 (Fig. 4*B* and *SI Appendix*, Fig. S7*B*).

Structural Plasticity of the Human PD-1 Ligand-Binding Interface. To further investigate how the observed loop changes are associated with pocket formation, we superimposed the apo and PD-L2–bound structures of our human triple-mutant PD-1 (Fig. 4*C*). Upon binding PD-L2, a large conformational change occurs in the PD-1 ligand-binding interface (Fig. 4*C*). A three-residue shortening of βC occurs (*SI Appendix*, Fig. S7*C*), and βC and βF move apart to create a deep cleft (Fig. 4*C*). The rearrangements in the pocket propagate to the edge of the FG loop, resulting in a remarkable 8.2 Å lateral shift (Fig. 4*C*).

We note that the overall change is less dramatic in murine PD-1 (*SI Appendix*, Fig. S7*D*). The closed architecture of the murine pocket does not require flipping of residues E84 and F63, as seen in human PD-1, and there is no secondary structure change in βC in murine PD-1 (*SI Appendix*, Fig. S7*E*). Taken together, our results provide a structural basis for systematic rearrangements at the human PD-1 ligand-binding interface that couple pocket formation and changes in the loops of PD-1 when it binds PD-L2.

Discussion

A prominent pocket forms in human PD-1 upon binding PD-L2. This pocket has a volume of 170 Å^3, comparable to pockets that bind small-molecule drugs (22, 23, 40, 41). The structure of this pocket is quite distinct from the corresponding pocket in murine PD-1 bound to PD-L2 (21).

We speculate that this pocket represents an attractive drug target. How would a pocket-binding drug bind to a flat protein surface? We conceptualize an ensemble of PD-1 conformations (*SI Appendix*, Fig. S8) in which the predominant species of apo-PD-1 has a flat ligand-binding surface ($K_i < 1$). A pocket-binding drug will stabilize the PD-1 conformation containing the pocket (K_{iii}). Drug binding via an induced-fit mechanism ($K_{iv} > 1$) can also occur.

The human PD-1/PD-L2 structure reported here will facilitate virtual drug screening to identify potential lead compounds (e.g., ref. 28). Specifically, we envision a small molecule binding to PD-1 contacting all or many of the residues that form the pocket, particularly F63, V64, N66, Y68, E84, L122, G124, I126, I134, and E136 in a conformation similar to that formed in the complex with PD-L2 (Fig. 3*D*). In addition, the structures of the indole and phenol rings and neighboring side chains of PD-L2 when bound to the pocket (Fig. 3*E*) are potentially useful starting points for the design of fragment-based screening scaffolds (42).

Since the PD-1 pocket is not populated substantially in the absence of PD-L2, it is not straightforward to use traditional drug-screening methods to identify small molecules that bind the pocket. Nonetheless, we speculate that conformational changes in the CC′ and FG loops and formation of pockets in the ligand-binding interface of PD-1 are thermodynamically coupled (Fig. 4*D*) and that this coupling can be used to enable drug-discovery efforts. We envision that PD-1 exists in an ensemble of conformations in the absence of ligands, populating predominantly structures that contain a flat ligand-binding face (i.e., $K_1 < 1$). PD-1 molecules with a preformed pocket have a higher affinity for PD-L2 ($K_3 > K_2$). Thermodynamics dictates that $K_1\ K_3 = K_2\ K_4$, so $K_4 > K_1$. In this model, the PD-1 loop variants studied here

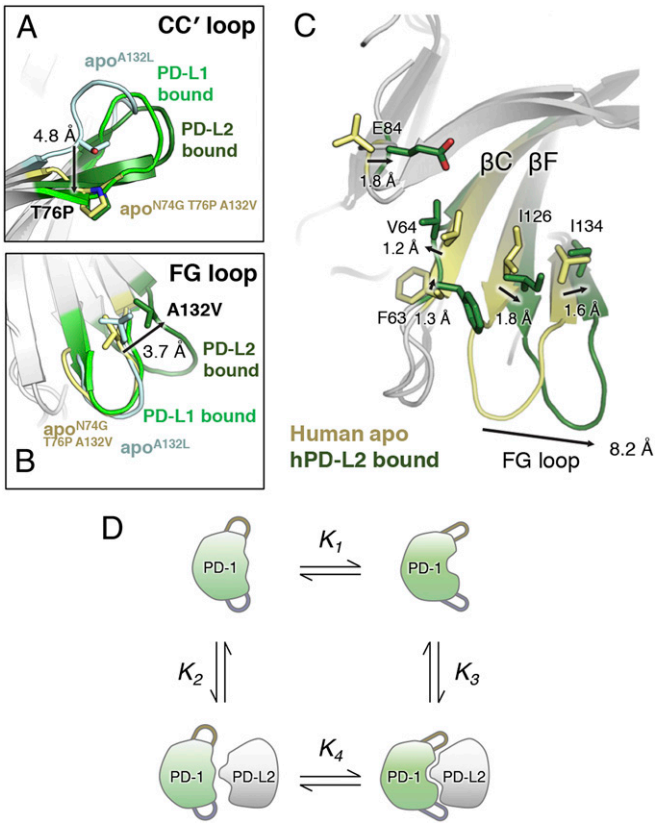

Fig. 4. PD-L2 binding induces conformational changes in the CC′ and FG loops of human PD-1. (*A* and *B*) The CC′ and FG loops change conformations. Overlays of ribbon diagrams of the CC′ loops (*A*) and the FG loops (*B*) from human apo-PD-1^{A132L} (PDB ID code: 3RRQ, cyan), apo-PD-1$^{N74G\ T76P\ A132V}$ (pale yellow), PD-L1–bound PD-1 (PDB ID code: 4ZQK, bright green), and PD-L2–bound PD-1$^{N74G\ T76P\ A132V}$ (dark green). (*A*) T76 of apo-PD-1, as well as P76 of apo-PD-1$^{N74G\ T76P\ A132V}$ and PD-L2–bound PD-1$^{N74G\ T76P\ A132V}$, are indicated with sticks. The arrow highlights a 4.8-Å C_α shift for residue 76 (T-to-P) from apo-PD-1^{A132L} to apo-PD-1$^{N74G\ T76P\ A132V}$. (*B*) L132 of apo-PD-1^{A132L}, as well as V132 of apo-PD-1$^{N74G\ T76P\ A132V}$ and PD-L2–bound PD-1$^{N74G\ T76P\ A132V}$, are indicated with sticks. The arrow highlights a 3.7-Å C_α shift for V132 from apo-PD-1$^{N74G\ T76P\ A132V}$ to PD-L2–bound PD-1$^{N74G\ T76P\ A132V}$. (*C*) Pocket formation is associated with the loop change. Overlay of ribbon diagrams of human apo-PD-1$^{N74G\ T76P\ A132V}$ (pale yellow) and PD-L2–bound PD-1$^{N74G\ T76P\ A132V}$ (dark green). A subset of pocket residues that undergo main-chain rearrangements (arrows) are indicated with sticks. Distances of C_α shifts from the unbound to the PD-L2–bound states are indicated. The FG loop shift of 8.2 Å for human PD-1 was measured using the C_α of P130. (*D*) A thermodynamic cycle for PD-1 binding PD-L2. For clarity, only two of the states in the conformational ensemble of apo-PD-1 (*Upper*) are depicted. In one of these states (*Left*), the ligand-binding interface is flat. In the second state (*Right*), a pocket is formed and the loops have moved. Mutations or external agents (e.g., antibodies) could stabilize the loops in the PD-L2 bound conformation (i.e., increase K_1), thereby increasing the population of apo-PD-1 molecules in the bound conformation. Equilibrium constants for each step in the thermodynamic cycle are indicated (see *Discussion*).

increase K_1 and lead to a higher proportion of apo-PD-1 in the PD-L2–bound conformation.

The higher association constants (k_{on}) for binding ligands by the mutant PD-1, as compared to WT PD-1 (Fig. 2*G* and *SI Appendix*, Fig. S2*C*), support this model. Such kinetic properties are consistent with an increased fraction, relative to WT PD-1, of unliganded mutant PD-1 molecules that are in a ligand-bound conformation (ref. 32; see, however, ref. 33). In addition, the CC′ loop shifts toward the PD-L2–bound conformation in the apo-PD-1 triple and double mutants (*SI Appendix*, Fig. S7*A*). (While there are only minimal changes in the pocket in both apo-PD-1 mutants [Fig. 3*C*], the pocket residues and a neighboring FG loop have substantial crystal contacts in the lattice [*SI Appendix*, Fig. S5*H*] that likely interfere with conformational changes.)

Coupling between the pocket and the loops would stabilize the pocket in the absence of a ligand, for example if the loops were held in their PD-L2–bound conformations with antibodies or aptamers. Alternatively, or in addition, new mutations (e.g., amino acid replacements, insertions, and/or deletions) could be selected for or designed to induce conformational changes in the loops. This coupling could therefore enable more traditional approaches to small-molecule drug discovery, such as high-throughput screening (22, 43–45) and/or the discovery of allosteric regulators of PD-1 activity. More generally, our work has implications for enhancing discovery of small-molecule inhibitors of other "undruggable" protein–protein interactions.

Materials and Methods

Additional information is provided in *SI Appendix*, *SI Materials and Methods*.

Protein Expression and Crystallization. The human apo-PD-1$^{N74G\ T76P\ A132V}$ and human apo-PD-1$^{T76P\ A132V}$ proteins (*SI Appendix*, Table S2) were overexpressed in and refolded from the inclusion bodies of *Escherichia coli* BL21(DE3) (Invitrogen). The human apo-PD-1$^{N74G\ T76P\ A132V}$ protein was crystallized in 100 mM NaCl, 100 mM Tris:HCl pH 8.0, and 27% (wt/vol) PEG-MME 5000. The human apo-PD-1$^{T76P\ A132V}$ protein was crystallized in 100 mM NaCl, 100 mM Tris:HCl pH 8.0, and 36% (wt/vol) PEG 3350. The human PD-1$^{N74G\ T76P\ A132V}$ and human PD-L2^{IgV} protein complex (*SI Appendix*, Table S2) was produced using the human Expi293F cell line (Gibco). The complex was crystallized in 200 mM magnesium acetate and 10% (wt/vol) PEG 8000.

ACKNOWLEDGMENTS. We thank Drs. J. S. Fraser and J. S. Weissman for helpful comments on an earlier version of this manuscript; members of the P.S.K. laboratory, especially B. N. Bell, T. U. J. Bruun, M. V. F. Interrante, P. A. Weidenbacher, and Drs. L. N. Deis, Y. Hwang Fu, L. W. H. Lee, and A. E. Powell for discussion and helpful comments on the manuscript; Drs. J. S. Fraser, J. D. Bloom, and L. Zhang for insightful discussion and technical expertise; Dr. J. R. Cochran for access to a flow cytometer; and Dr. D. Fernandez of the Stanford ChEM-H Macromolecular Structure Knowledge Center and staff scientists of the Stanford Synchrotron Radiation Lightsource (SSRL) beam lines 12-2 and 14-1 for X-ray crystallographic data collection. Use of the SSRL, SLAC National Accelerator Laboratory, is supported by the US Department of Energy (DOE), Office of Science, Office of Basic Energy Sciences under Contract DE-AC02-76SF00515. The SSRL Structural Molecular Biology Program is supported by the DOE Office of Biological and Environmental Research and by NIH National Institute of General Medical Sciences (NIGMS) Grant P41GM103393. This work was supported by the Emerson Collective Cancer Research Fund, NIH Grant DP1 DA043893, the Virginia and D. K. Ludwig Fund for Cancer Research, and the Chan Zuckerberg Biohub. S.T. is a Merck Fellow of the Damon Runyon Cancer Research Foundation, DRG-2301-17.

1. C. Robert *et al.*; KEYNOTE-006 investigators, Pembrolizumab versus ipilimumab in advanced melanoma. *N. Engl. J. Med.* **372**, 2521–2532 (2015).
2. H. Borghaei *et al.*, Nivolumab versus docetaxel in advanced nonsquamous non-small-cell lung cancer. *N. Engl. J. Med.* **373**, 1627–1639 (2015).
3. D. J. Byun, J. D. Wolchok, L. M. Rosenberg, M. Girotra, Cancer immunotherapy–immune checkpoint blockade and associated endocrinopathies. *Nat. Rev. Endocrinol.* **13**, 195–207 (2017).
4. D. T. Le *et al.*, Mismatch repair deficiency predicts response of solid tumors to PD-1 blockade. *Science* **357**, 409–413 (2017).
5. L. Marcus, S. J. Lemery, P. Keegan, R. Pazdur, FDA approval summary: Pembrolizumab for the treatment of microsatellite instability-high solid tumors. *Clin. Cancer Res.* **25**, 3753–3758 (2019).
6. A. I. Minchinton, I. F. Tannock, Drug penetration in solid tumours. *Nat. Rev. Cancer* **6**, 583–592 (2006).
7. E. A. Neuwelt *et al.*, Engaging neuroscience to advance translational research in brain barrier biology. *Nat. Rev. Neurosci.* **12**, 169–182 (2011).
8. J. L. Mikitsh, A. M. Chacko, Pathways for small molecule delivery to the central nervous system across the blood-brain barrier. *Perspect. Medicin. Chem.* **6**, 11–24 (2014).

9. Y. Wang *et al*., Treatment-related adverse events of PD-1 and PD-L1 inhibitors in clinical trials: A systematic review and meta-analysis. *JAMA Oncol.* **5**, 1008–1019 (2019).
10. A. Shimabukuro-Vornhagen *et al*., Cytokine release syndrome. *J. Immunother. Cancer* **6**, 56 (2018).
11. R. J. Keizer, A. D. Huitema, J. H. Schellens, J. H. Beijnen, Clinical pharmacokinetics of therapeutic monoclonal antibodies. *Clin. Pharmacokinet.* **49**, 493–507 (2010).
12. L. L. Brunton, R. Hilal-Dandan, B. C. Knollmann, *Goodman & Gilman's the Pharmacological Basis of Therapeutics* (McGraw-Hill Education, 2018).
13. M. E. Krause, E. Sahin, Chemical and physical instabilities in manufacturing and storage of therapeutic proteins. *Curr. Opin. Biotechnol.* **60**, 159–167 (2019).
14. P. Jiao *et al*., Small molecules as PD-1/PD-L1 pathway modulators for cancer immunotherapy. *Curr. Pharm. Des.* **24**, 4911–4920 (2018).
15. H. Dong, G. Zhu, K. Tamada, L. Chen, B7-H1, a third member of the B7 family, co-stimulates T-cell proliferation and interleukin-10 secretion. *Nat. Med.* **5**, 1365–1369 (1999).
16. Y. Latchman *et al*., PD-L2 is a second ligand for PD-1 and inhibits T cell activation. *Nat. Immunol.* **2**, 261–268 (2001).
17. K. M. Zak *et al*., Structural biology of the immune checkpoint receptor PD-1 and its ligands PD-L1/PD-L2. *Structure* **25**, 1163–1174 (2017).
18. X. Cheng *et al*., Structure and interactions of the human programmed cell death 1 receptor. *J. Biol. Chem.* **288**, 11771–11785 (2013).
19. K. M. Zak *et al*., Structure of the complex of human programmed death 1, PD-1, and its ligand PD-L1. *Structure* **23**, 2341–2348 (2015).
20. D. Y. Lin *et al*., The PD-1/PD-L1 complex resembles the antigen-binding Fv domains of antibodies and T cell receptors. *Proc. Natl. Acad. Sci. U.S.A.* **105**, 3011–3016 (2008).
21. E. Lázár-Molnár *et al*., Crystal structure of the complex between programmed death-1 (PD-1) and its ligand PD-L2. *Proc. Natl. Acad. Sci. U.S.A.* **105**, 10483–10488 (2008).
22. M. R. Arkin, Y. Tang, J. A. Wells, Small-molecule inhibitors of protein-protein interactions: Progressing toward the reality. *Chem. Biol.* **21**, 1102–1114 (2014).
23. K. A. Loving, A. Lin, A. C. Cheng, Structure-based druggability assessment of the mammalian structural proteome with inclusion of light protein flexibility. *PLoS Comput. Biol.* **10**, e1003741 (2014).
24. X. Zhang *et al*., Structural and functional analysis of the costimulatory receptor programmed death-1. *Immunity* **20**, 337–347 (2004).
25. J. D. Bloom, An experimentally determined evolutionary model dramatically improves phylogenetic fit. *Mol. Biol. Evol.* **31**, 1956–1978 (2014).
26. D. M. Fowler, S. Fields, Deep mutational scanning: A new style of protein science. *Nat. Methods* **11**, 801–807 (2014).
27. G. Chao *et al*., Isolating and engineering human antibodies using yeast surface display. *Nat. Protoc.* **1**, 755–768 (2006).
28. J. Lyu *et al*., Ultra-large library docking for discovering new chemotypes. *Nature* **566**, 224–229 (2019).
29. E. Lázár-Molnár *et al*., Structure-guided development of a high-affinity human Programmed Cell Death-1: Implications for tumor immunotherapy. *EBioMedicine* **17**, 30–44 (2017).
30. R. L. Maute *et al*., Engineering high-affinity PD-1 variants for optimized immunotherapy and immuno-PET imaging. *Proc. Natl. Acad. Sci. U.S.A.* **112**, E6506–E6514 (2015).
31. Y. Li *et al*., High-affinity PD-1 molecules deliver improved interaction with PD-L1 and PD-L2. *Cancer Sci.* **109**, 2435–2445 (2018).
32. I. H. Moal, P. A. Bates, Kinetic rate constant prediction supports the conformational selection mechanism of protein binding. *PLoS Comput. Biol.* **8**, e1002351 (2012).
33. K. G. Daniels, Y. Suo, T. G. Oas, Conformational kinetics reveals affinities of protein conformational states. *Proc. Natl. Acad. Sci. U.S.A.* **112**, 9352–9357 (2015).
34. S. Tang, P. S. Kim, A high-affinity human PD-1/PD-L2 complex informs avenues for small-molecule immune checkpoint drug discovery. bioRxiv:10.1101/786319 (29 September 2019).
35. J. Y. Lee *et al*., Structural basis of checkpoint blockade by monoclonal antibodies in cancer immunotherapy. *Nat. Commun.* **7**, 13354 (2016).
36. S. Horita *et al*., High-resolution crystal structure of the therapeutic antibody pembrolizumab bound to the human PD-1. *Sci. Rep.* **6**, 35297 (2016).
37. Z. Na *et al*., Structural basis for blocking PD-1-mediated immune suppression by therapeutic antibody pembrolizumab. *Cell Res.* **27**, 147–150 (2017).
38. R. Pascolutti *et al*., Structure and dynamics of PD-L1 and an ultra-high-affinity PD-1 receptor mutant. *Structure* **24**, 1719–1728 (2016).
39. J. Yu, Y. Zhou, I. Tanaka, M. Yao, Roll: A new algorithm for the detection of protein pockets and cavities with a rolling probe sphere. *Bioinformatics* **26**, 46–52 (2010).
40. A. J. Souers *et al*., ABT-199, a potent and selective BCL-2 inhibitor, achieves antitumor activity while sparing platelets. *Nat. Med.* **19**, 202–208 (2013).
41. C. Tovar *et al*., MDM2 small-molecule antagonist RG7112 activates p53 signaling and regresses human tumors in preclinical cancer models. *Cancer Res.* **73**, 2587–2597 (2013).
42. D. A. Erlanson, S. W. Fesik, R. E. Hubbard, W. Jahnke, H. Jhoti, Twenty years on: The impact of fragments on drug discovery. *Nat. Rev. Drug Discov.* **15**, 605–619 (2016).
43. R. Macarron *et al*., Impact of high-throughput screening in biomedical research. *Nat. Rev. Drug Discov.* **10**, 188–195 (2011).
44. D. E. Scott, A. R. Bayly, C. Abell, J. Skidmore, Small molecules, big targets: Drug discovery faces the protein-protein interaction challenge. *Nat. Rev. Drug Discov.* **15**, 533–550 (2016).
45. S. Hoelder, P. A. Clarke, P. Workman, Discovery of small molecule cancer drugs: Successes, challenges and opportunities. *Mol. Oncol.* **6**, 155–176 (2012).